Article

Atmospheric Cold Front-Generated Waves in the Coastal Louisiana

Yuhan Cao [1] (iD), Chunyan Li [2],* and Changming Dong [1,3],*

[1] School of Marine Sciences, Nanjing University of Information Science and Technology, Nanjing 210044, China; yhcao_nuist@163.com

[2] Department of Oceanography and Coastal Sciences, College of the Coast and Environment, Louisiana State University, Baton Rouge, LA 70803, USA

[3] Southern Laboratory of Ocean Science and Engineering (Zhuhai), Zhuhai 519000, China

* Correspondence: cli@lsu.edu (C.L.); cmdong@nuist.edu.cn (C.D.); Tel.: +1-225-578-2520 (C.L.); +86-025-58695733 (C.D.)

check for
updates

Abstract: Atmospheric cold front-generated waves play an important role in the air–sea interaction and coastal water and sediment transports. In-situ observations from two offshore stations are used to investigate variations of directional waves in the coastal Louisiana. Hourly time series of significant wave height and peak wave period are examined for data from 2004, except for the summer time between May and August, when cold fronts are infrequent and weak. The intra-seasonal scale variations in the wavefield are significantly affected by the atmospheric cold frontal events. The wave fields and directional wave spectra induced by four selected cold front passages over the coastal Louisiana are discussed. It is found that significant wave height generated by cold fronts coming from the west change more quickly than that by other passing cold fronts. The peak wave direction rotates clockwise during the cold front events. The variability of the directional wave spectrum shows that the largest spectral density is distributed at low frequency in the postfrontal phase associated with migrating cyclones (MC storms) and arctic surges (AS storms).

1. Introduction

Offshore and coastal waves can impact coastal infrastructure, shipping, marine operations, and marine energy extraction. Coastal and offshore engineering projects are significantly affected by the atmospheric cold front-generated waves. Investigation of offshore waves generated by atmospheric cold fronts is necessary for various applications, including sediment transport, coastal erosion prevention, coastal construction design, and pollution transport [1].

Coastal Louisiana lies along the northern Gulf of Mexico (GoM), with a coastline oriented roughly from east to west (Figure 1). The Louisiana coastal area, including the lower Mississippi River deltaic plain, comprises 40% of the United States wetland [2,3]. On different short- and long-term (temporal) and west to east (spatial) scales, the wind characteristics along the Louisiana coast are very different [4]. A land–sea breeze effect is apparent along the Louisiana coast all year round and is especially pronounced in the summer. On the intra-seasonal scale, wind pattern variabilities are due to the impact of hurricane and cold fronts. Cold fronts are usually characterized by a significant wind shear, a sharp drop in atmospheric pressure and a rapid decrease in air temperature. In the coastal Louisiana, cold fronts usually have a clockwise variation in wind direction at a fixed location [5]. It has been believed that approximately 30–40 fronts per year pass over the northern Gulf—that is, one front every 3–10 days [6,7]. A recent study [8] for a 40-year record shows that there are 41.2 ± 4.7 fronts per

year, excluding May, June, July, and August when frontal activities reach the minimum. This gives a frontal recurring period of ~5.8 days.
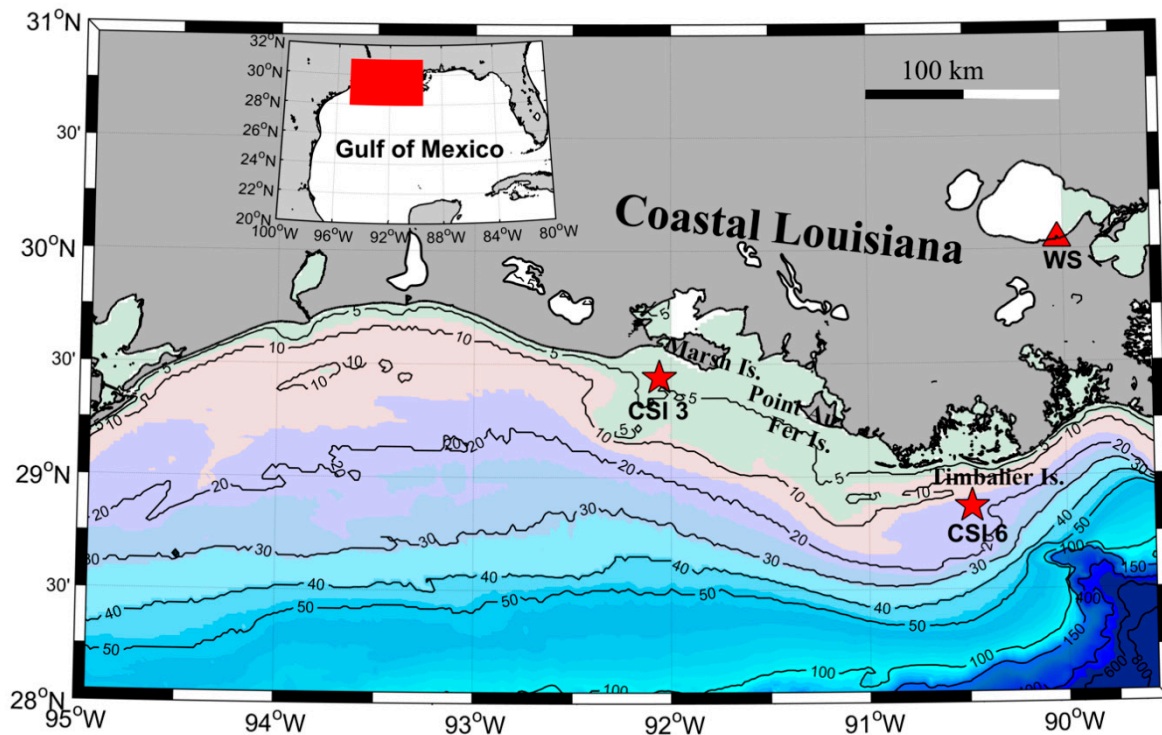

Figure 1. Study area. Contour is the bathymetry (unit: m) from ETOPO1. The red five-pointed stars represent the WAVCIS (http://www.wavcis.lsu.edu/) stations. CSI 3 is off the Marsh Island and the CSI 6 is south of Timbalier Island. The red triangle represents the weather station (WS). The inset shows the study area in southern Louisiana.

The maximum wave variability and wave energy occur during the passing of a cold front [9–14]. Although cold fronts are less extreme than hurricanes and the resulting wind wave height is much less than hurricane waves, they are frequent in fall, winter and spring, and the waves generated by the weather systems may cause damage to the coastal marine infrastructures. When waves occur in shallow waters, currents can transport suspended sediment whose redeposition may lead to siltation of ports, channels and estuaries. The influence of waves associated with cold fronts on sediment suspension may increase sediment concentration, due to the superposition of bottom shear stress generated by wind-induced waves and shelf currents [15]. Therefore, investigating the variations of nearshore waves is necessary for a variety of applications, including the estimation of sediment transport, coastal erosion prevention, coastal construction design and calculation of transport of pollutants [16–19].

Using model and in-situ data, Stone et al. [20] studied the wave and wind variations during a cold front that crossed the north-central part of the GoM. They pointed out that significant wave heights during frontal activity mostly persist in the high-frequency band, and the nonlinear wave–wave interaction play a dominant role. Waves respond to rapidly evolving winds during the prefrontal phase in the northern GoM [21]. Chaichitehrani et al. [15] numerically simulated the effect of wind-generated waves on sediment dynamics in the northern GoM and proposed that the shear stress from wave motions during the storms was the dominant force in the resuspension of sediments. Wave energy is a key factor in coastal engineering applications. The evolution of the energy spectra, when a cold front is crossing the south-central Louisiana, is quite abrupt, and the dominant direction shifted from southwest to north across the shoal, as suggested by Jose et al. [22]. Appendini et al. [13] calculated wave power by using a wave model and characterized each cold front (anticyclonic cold surge). They concluded that the waves resulted from the wind intensity, duration of the storm and the

fetch. Sorourian et al. [23] predicted a larger magnitude of wave spectral densities during cold front events than persistent southeasterly wind events, using the FVCOM- SWAVE model. Despite these efforts, cold front characteristics and their impacts of cold fronts on waves on a longer time scale—e.g., over one year—has not yet been discussed.

This work focuses on directional wave and wave energy propagation in response to cold fronts in coastal Louisiana. The main objectives are to investigate the two-dimensional wave directional spectrum and temporal variability from in-situ wave field data obtained during cold front events in 2004 excluding the time from 1 May 1 to 31 August, due to weak frontal activities in these months. Using hourly observational data, ocean wave processes under the influence of cold fronts can be better demonstrated. A description of the method and data is presented in Section 2. In Section 3, observations, including significant wave height (*Hs*), peak wave direction (*Dp*) and peak wave period (*Tp*), are presented, and the wave energy, including the directional and frequency, is discussed. Section 4 provides a discussion of the results. The conclusions of the work are presented in Section 5.

2. Materials and Methods

In order to determine the mechanism and dynamical processes of the atmospheric cold front-generated waves in the coastal Louisiana, this study applies directional wave spectrum analysis and statistical analysis to the in-situ observations.

2.1. Wave Parameter and Wave Spectra Data

The wave data employed in this paper are observed from two Wave-Current-Surge Information System (WAVCIS) stations (CSI 3 and CSI 6) of Louisiana State University. WAVCIS is a permanent and real-time ocean observing system along the Louisiana coast [24]. The Teledyne RD Instrument Acoustic Doppler Current Profiler (ADCP) is used to measure directional waves at WAVCIS stations. Waves measured by the ADCP are calculated by its associated software WavesMon [25].

The CSI 3 is located at 29.441° N, 92.061° W, which is 18 km south of Marsh Island. The depth at CSI 3 is approximately 5 m. The CSI 6 is located at 28.867° N, 90.483° W, which is 20 km south of Timbalier Island. The depth at CSI 6 is approximately 20 m (Figure 1). The stations constantly experience the combined effects of wind-driven waves and swells from deep water. The sampling rate is 2 Hz for 2048 bursts. The wave data are provided at hourly intervals. The time range of the CSI 3 data includes January, February, March, April, September, October, November and December of 2004, while that of CSI6 includes September, November and December of 2004.

The directional wave spectra measured by the ADCP at CSI 3 and CSI 6 reveal the interaction of swells and wind-driven waves. The WAVCIS stations use 0.15 to 0.2 Hz frequency as the separation criterion to estimate swells and wind-waves.

The directional wave spectrum is separated into a frequency spectrum and a directional spreading function [26], as follows:

$$E(\omega, \theta) = S(\omega)D(\omega, \theta) \tag{1}$$

where $\omega = 2\pi f$ (*f* is the fundamental frequency) is the angular frequency of the wave and θ is the wave propagation angle. $S(\omega)$ is the wave frequency spectrum and $D(\omega,\theta)$ is the directional distribution. The directional distribution is often normalized by:

$$\int_0^{2\pi} D(\omega, \theta) = 1, \omega \geq 0 \tag{2}$$

The directional coefficients, c_n, are defined as the Fourier coefficients in the expansion of the frequency-direction spectrum:

$$D(\omega, \theta) = \frac{1}{2\pi} \sum_{-\infty}^{+\infty} c_n(\omega) \exp(-in\theta) \tag{3}$$

where n indicates the beam number. By calculating the coefficients, the cross-spectrum between sensors in the ADCP can be obtained. The cross-spectrum has a linear relationship with the directional spectrum, and the directional spectrum can be obtained by inversion.

2.2. Meteorological Data

An atmospheric front is a largescale atmospheric circulation. The atmospheric parameters are measured at the Southern Lake Pontchartrain (30.0424° N, 90.0282° W), which is a local airport (red triangles in Figure 1). The data are obtained from the National Weather Service. The hourly time series data include a time period in 2004 excluding the time from 1 May to 31 August. Measured data include wind speed (ms^{-1}), wind direction (degree), surface atmospheric pressure (hPa) and temperature (centigrade).

2.3. CCMP Wind Vector Analysis Product

Six-hourly wind speed and wind direction are provided by the Cross-Calibrated Multi-Platform (CCMP), which has a horizontal resolution of 0.25° × 0.25°. The domain of the wind field is between latitudes 28°–31° N and longitudes 89.5°–95° W. The CCMP gridded surface vector winds are produced using satellite, moored buoy and model wind data, and as such, they are considered to be a Level-3 ocean vector wind analysis product. The CCMP Version 2.0 (V2) data product described here is a continuation of the widely-used original CCMP product and builds on the decades of Variational Analysis Method (VAM) development [27].

2.4. Low-Pass Filtered and Correlation Analysis

The hourly wind speed, temperature and wave data are low-pass filtered to retain the intra-seasonal variations. The time series data are lowpass filtered by a fast Fourier transform (FFT) algorithm with a cutoff frequency of 0.6 CPD (cycle per day) or equivalently, a 40-h filter. FFT is generally used to find the frequency components of the signal buried in the noisy time domain signal [28,29].

The skill metrics selected in this study is the correlation coefficient (CC); the formulation is as follows:

$$CC = \frac{\sum_{i=1}^{N}(X_i - Xmean)(Y_i - Ymean)}{\sqrt{\sum_{i=1}^{N}(X_i - Xmean)^2 \sum_{i=1}^{N}(Y_i - Ymean)^2}} \tag{4}$$

where X_i and Y_i denote observed wind data and wave data, respectively, and N is the total number of observations. *Xmean* and *Ymean* indicate the mean values of observed wind data and wave data, respectively. The *CC* is the Pearson product–moment correlation coefficient and has a value between −1 and 1, with a unit value indicating perfect correlation and 0 meaning no correlation [30].

3. Results

3.1. Intra-Seasonal Variation of Atmospheric Parameters and Wave

A cold front can be extended from the center of a low air pressure system to thousands of kilometers (2000–3000 km). The spatial scales of atmospheric cold fronts are much larger than those of hydrodynamics in estuaries and the coastal ocean [31]. A cold front event has three basic phases: the prefrontal, frontal passage and postfrontal or cold air outbreak phases. Intra-seasonal variations are prominent in the coastal Louisiana atmospheric cold frontal events. By examining the surface weather maps, a total of 37 atmospheric cold frontal events occurred in coastal Louisiana in 2004, excluding May, June, July and August (Table 1). The average monthly number of atmospheric cold frontal events affecting the Louisiana coast over a 40-year record ranges from 3 (September) to 6.3 (January) [8]. Atmospheric cold fronts along the Louisiana coast can be roughly categorized into two end-member types: (a) arctic surges (AS storm), which are less frequent, more powerful and moving southward, affect the entire Louisiana coast almost simultaneously because the orientations of those fronts are

typically parallel to the coastline; (b) migrating cyclones (MC storm), which are accompanied by a strong low-pressure system (cyclone) and have fairly strong southerly winds before the frontal passage, followed by strong northwesterly winds [32,33]. There are five AS storms and 32 MC storms, as shown in Table 1. Table 1 shows cold fronts generally come from four directions: northwest (18 events), west (nine events), north (seven events) and northeast (three events).

Table 1. Atmospheric cold fronts from the daily weather maps of the National Centers for Environmental Prediction, Weather Prediction Center in 2004, excluding May, June, July and August.

Month	Date (12 A.M. UTC)	Moving Direction	Atmospheric Pressure (hPa)	Type
Jan.	05	NW	1016	MC storm [1]
	09	NW	1020	MC storm
	15	N	1018	AS storm [2]
	18	W	1008	MC storm
	30	NW	1014	MC storm
Feb.	02	W	1014	MC storm
	06	W	1012	MC storm
	12	NW	1016	MC storm
	21	NW	1016	MC storm
Mar.	06	NW	1018	MC storm
	13	N	1022	MC storm
	16	NW	1015	MC storm
	21	N	1022	AS storm
	29	NW	1021	MC storm
Apr.	03	NE	1016	MC storm
	05	N	1016	AS storm
	09	N	1010	MC storm
	12	W	1007	MC storm
	26	NW	1016	MC storm
Sep.	07	NW	1010	MC storm
	10	N	1016	MC storm
	18	NE	1014	MC storm
	29	NW	1014	MC storm
Oct.	05	NW	1019	AS storm
	10	W	1004	MC storm
	12	NW	1012	MC storm
	14	W	1010	MC storm
Nov.	03	W	1014	MC storm
	08	N	1018	MC storm
	10	NE	1021	AS storm
	11	NW	1018	MC storm
	24	W	1006	MC storm
	27	NW	1011	MC storm
	30	W	1015	MC storm
Dec.	07	NW	1014	MC storm
	09	NW	1012	MC storm
	13	NW	1018	MC storm

[1] migrating cyclones (MC storm). [2] arctic surges (AS storm).

The cold-front associated atmospheric pressure and temperature variations exhibit a return period of about 3–7 days. There is usually a strong wind shear and sharp temperature and humidity gradients along a cold front. The minimum air temperature (approximately 5–12 °C) occurred after the cold frontal passages when the air pressure first dropped to its minimum (approximately 1006–1022 hPa) as shown in Figure 2a. The correlation coefficient between the air pressure and air temperature is −0.37. The temperature range under the influence of the cold front was about 15–20 °C (10–15 °C) in January

and February (March and April). In September and October, the atmospheric pressure experienced a significant reduction but was not accompanied by drastic changes in air temperature during the passage of a tropical cyclone (Figure 3a). The correlation coefficient between the air pressure and air temperature is −0.62. The mean daily air temperature varied between 22 and 32 °C in September and October. The temperature dropped sharply by about 18–24 °C under the influence of the cold front in November and December. The variations of wind speed presented diurnal and intra-seasonal oscillations. The timing of a frontal passage was closely related to strong winds. The maximum wind speed from January to April was 15 ms^{-1} (Figure 2b). The wind speed varied greatly between 1 and 17 ms^{-1} during September–December 2004 as shown in Figure 3b.
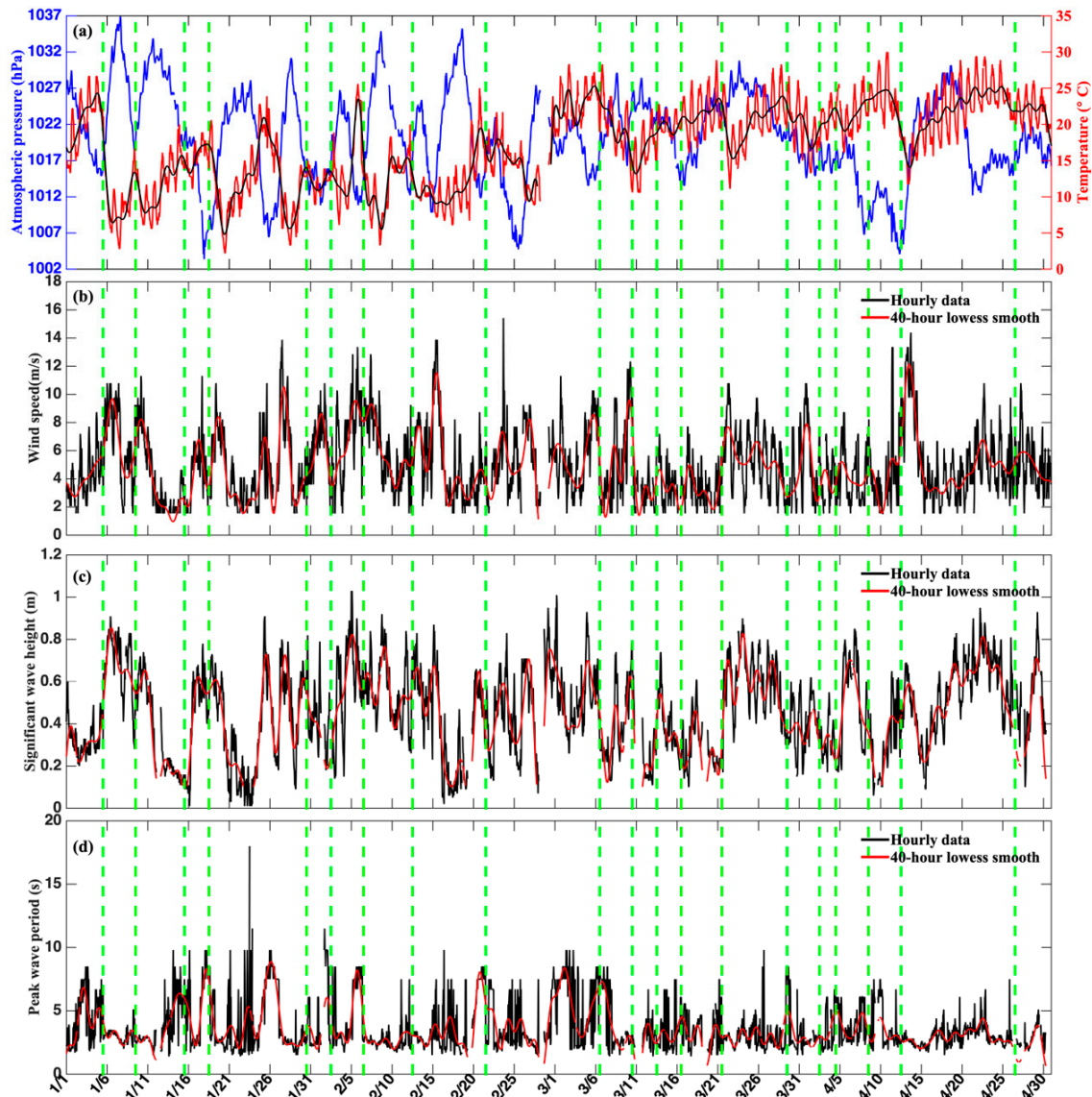

Figure 2. (**a**) Time series of the atmospheric pressure (blue line) and air temperature (red line) from the WS (30.0424° N, 90.0282° W) in Figure 1. The black line is the 40-h low pass filtered air temperature from January to April. (**b**) Wind speed (black line; unit: ms^{-1}) at WS, (**c**) significant wave height (black line; unit: m) and (**d**) peak wave period (black line; unit: s) at CSI 3 from January to April. The red line is the 40-h low pass filtered curve. The green vertical dashed lines indicate the timing of cold fronts.
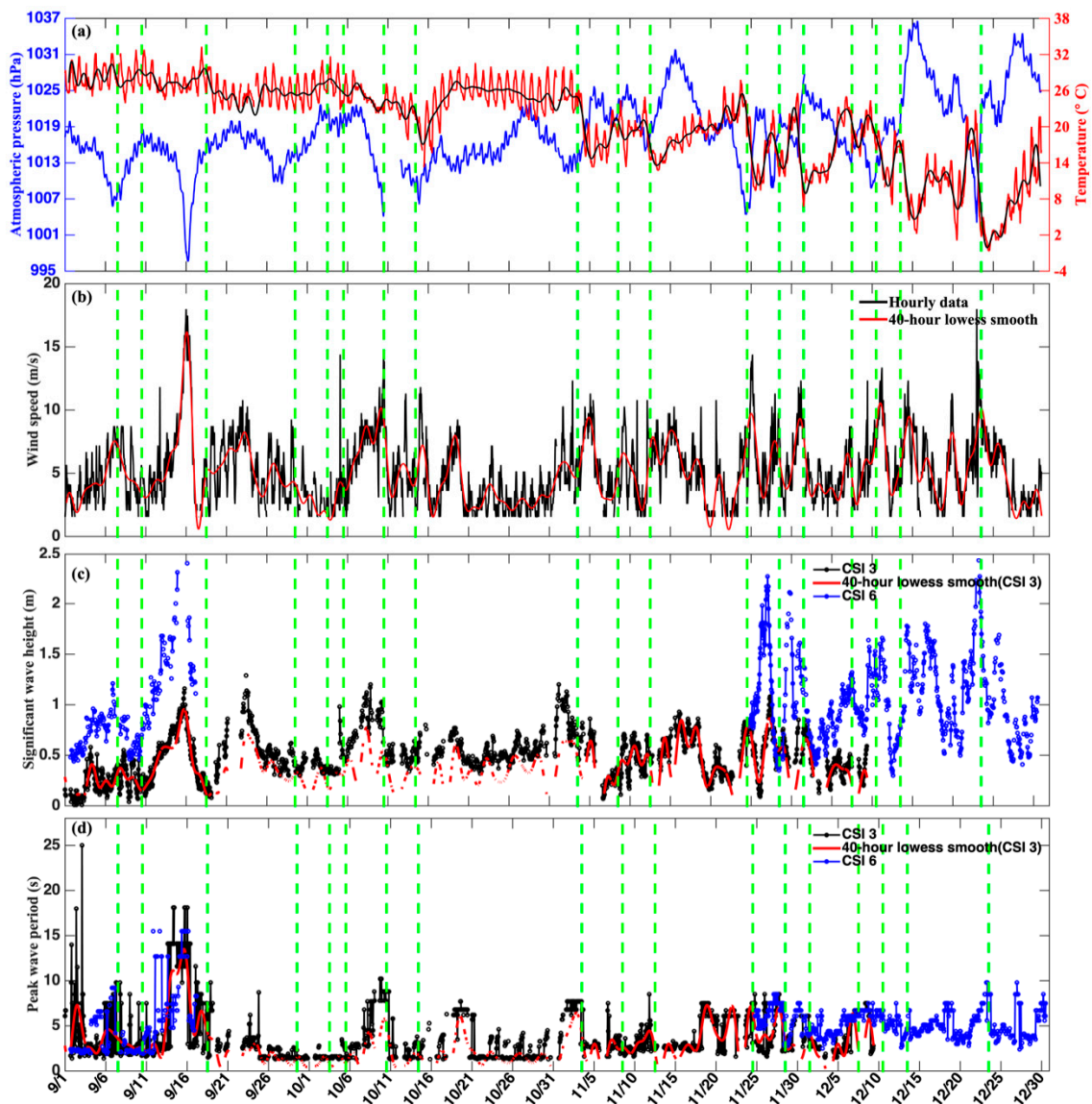
Figure 3. (**a**) Time series of the atmospheric pressure (blue line) and air temperature (red line) from the WS in Figure 1. The black line is the 40-h low pass filtered of air temperature September to December. (**b**) Wind speed (black line; unit: ms^{-1}) at WS, (**c**) significant wave height (black line for CSI 3 and blue line for CSI 6; unit: m) and (**d**) peak wave period (unit: s) from September to December. The red line is the 40-h low pass filtered data from CSI 3. The green vertical dashed lines indicate the timing of cold fronts.

Figure 2c shows the variation of the hourly *Hs* from January 1 to April 30 at station CSI 3. The maximum *Hs* was 1.1 m, and the average *Hs* was approximately 0.5 m during this period. The maximum *Hs* generally occurs by strong winds. The correlation coefficient between the *Hs* and wind speed at WS is 0.46. The wave height at both station CSI 3 and CSI 6 from September to December is shown in Figure 3c. *Hs* at the station CSI 3 is larger than that at station CSI 6, probably due to its shallower character and longer fetch during the southerly prefrontal winds. To further investigate the relationship of the waves in the coastal Louisiana with cold fronts, we applied a low-pass filter to remove the diurnal signals from the hourly *Hs*. It is clear that the wave field has an intra-seasonal oscillation (Figure 2c). The *Hs* becomes significantly higher during the passage of a cold front. The time series of observed *Hs* (Figure 3c), at CSI 3 (CSI 6) is less than 0.5 m (1 m) during the prefrontal phase and becomes larger when air pressure has a low value (corresponding to cold

front passage). Although there is a certain distance between the weather station and the wave station, the correlation coefficient between *Hs* at CSI 3 (CSI 6) and wind speed at WS is 0.46 (0.44). Figure 2d indicates that the highest *Tp* values correspond to the passage of cold fronts at CSI 3, and the maximum *Tp* is 18s. The variability of peak wave periods at the two stations is similar (Figure 3d). The peak wave period is related to wave energy.

3.2. Case Studies

In the Northern Hemisphere midlatitudes, the wind ahead of a cold front typically comes from the southeast, south or southwest. Behind the cold front, the wind is typically from the west or northwest. Figure 4 illustrates a schematic of the wind circulation in a cold front system. In order to better understand the influence of cold fronts on the Louisiana coast, four cases (5 January, 21 March, 24 November and 7 September) are selected for detailed analysis, by examining the surface weather maps and considering the quality and continuity of wave observation data. Variations of the hourly wind field from CCMP are shown in Figure 5. The spatial distribution of the wind field when the cold front passes in Case I (Figure 5a) on January 5 and Case III (Figure 5c) on November 24 are the typical winds in cold front systems (Figure 4). Figure 5b,d show that the wind fields are more complex during the passage of the cold fronts, which is due to the influence of other air pressure systems.

In Case I, the cold front came from the northwest (Figure 6f) with relatively strong prefrontal southerly winds (Figure 6i). This cold front is identified as that associated with a migrating cyclone. Affected by the cold front, wind directions in this case (Figure 6i) rotated clockwise from January 4 to 8. Wind speed (Figure 6a) and wave height (Figure 6b) increased when the front passed over the region. The correlation coefficient between the wind speed at the weather station (WS) and wave height at CSI 3 is 0.58. The maximum wave height 0.91 m appeared at 10:00 UTC on January 6. Figure 6c shows that the peak wave period was large during the prefrontal phase with dominantly southerly waves (Figure 6d). It should be noted that the peak wave period is associated with the most energetic waves in the wave spectrum at a specific point. Wind waves have shorter peak wave periods, and regions dominated by swells have longer peak wave periods. During cold front passages, waves along the Louisiana coast are dominated by wind waves. Waves come from the north with less nonlinear wave–wave interactions.
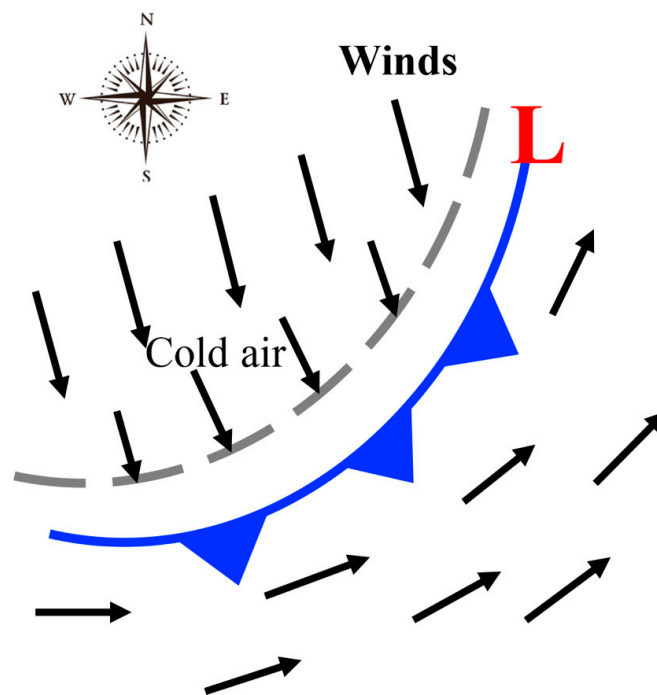

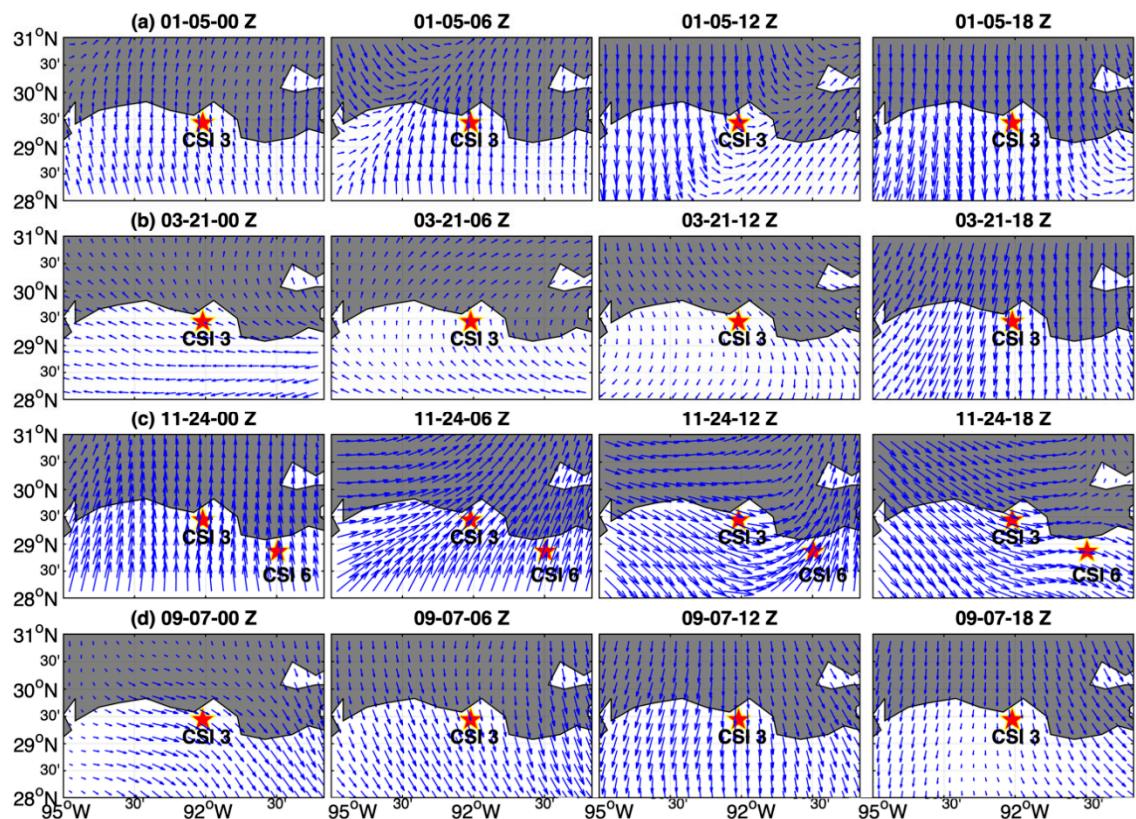**Figure 4.** Schematic figure of the cold front system and the wind shift at a cold front.

Figure 5. Spatial distribution of wind direction (blue arrows) from Cross-Calibrated Multi-Platform (CCMP) during the cold fronts passage for (**a**) Case I, (**b**) Case II, (**c**) Case III and (**d**) Case IV.

For coastal engineering applications, the influence of directional and frequency distributions of wave energy is generally more important than significant wave heights and wave periods [16]. Figure 7 shows the hourly two-dimensional wave directional spectrum encompassing the three frontal phases for Case I. Following the frontal passage, wave directions rotated clockwise from the south. In the prefrontal phase, the wave energy was from the south, and the peak value of directional spectrum was 0.7 m^2/Hz/cycle (Figure 7a). The wind wave was dominant in the prefrontal phase because of the much longer fetch of the GoM. The wave spectra were multi-modal with dominant directions between 180° and 210°, and separate peaks were induced by swell from the GoM and local wind-wave, respectively. Figure 7b displays that wave energy propagated from the north–northwest consistent with wind direction. The wave spectrum was mono-modal with a dominant direction at 330° at 14:00 UTC on 5 January. For the next several hours, most wave energies changed from high to low frequencies. The maximum wave energy appeared on 6 January in the postfrontal phase, and the peak value of directional spectrum was 6 m^2/Hz/cycle. The peak energy spectrum was between 0.2 and 0.4 Hz, while the spectrum between 0.4 and 0.6 Hz had smaller magnitudes (Figure 7c). Nonlinear triad–wave interactions in shallow water redistribute wave energy over the spectrum, transferring wave energy between high and low frequencies [17,34–36]. The wave directional spectrum was bi-modal with a large directional deviation on January 7. Wind speed (Figure 6a) started to decrease at 11:00 UTC on 7 January. Following the shift in wind direction, the peak energy dissipated. In the postfrontal phase, wind directions changed to southeast. The wave field had two principal components: the old northeast and the new southwest wave field. The wave spectrum was mono-modal with a dominant direction between 90° and 150° at 16:00 UTC on 7 January (Figure 7d).
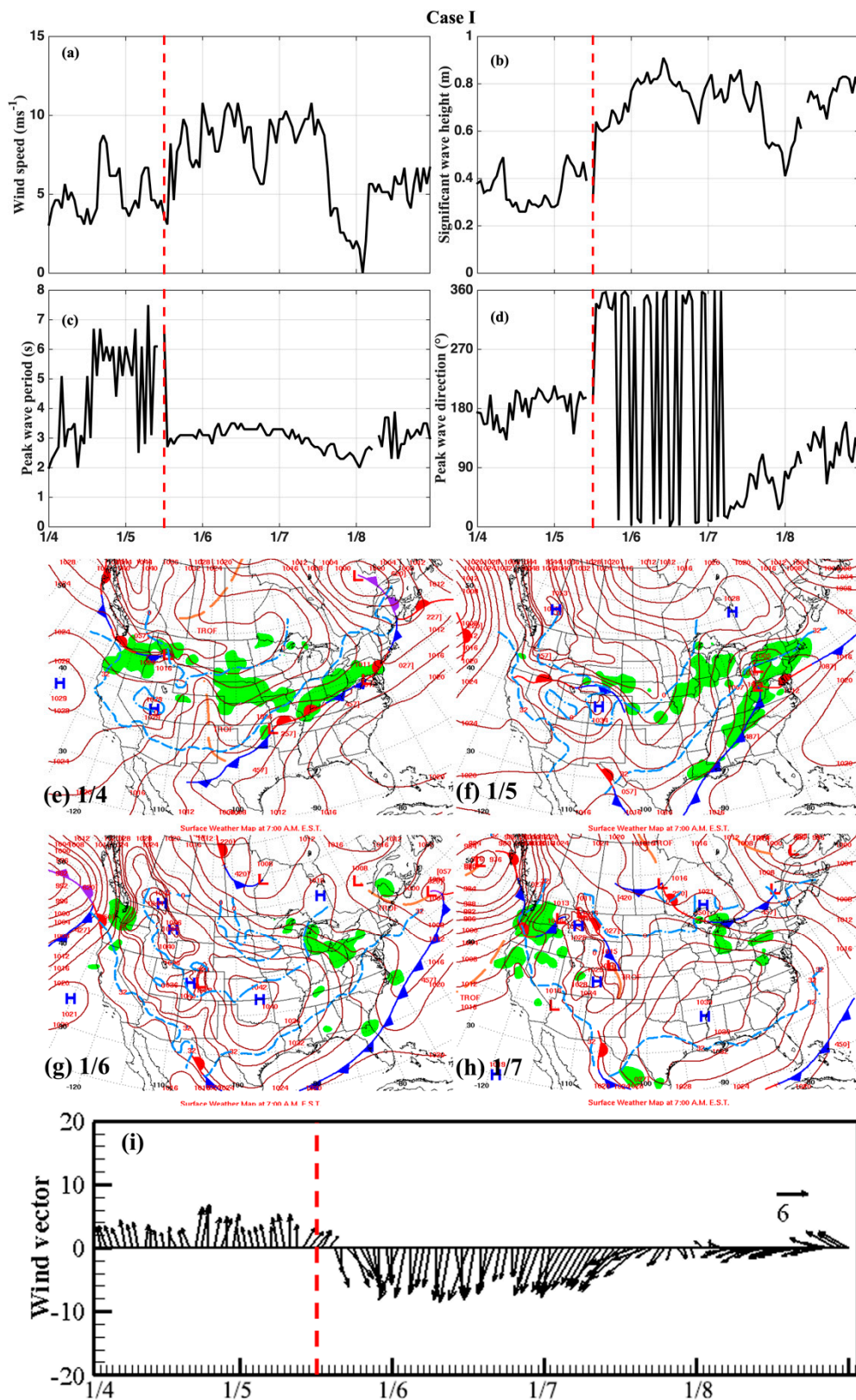
Figure 6. Case I: Time series of (**a**) wind speed (ms^{-1}), (**b**) significant wave height (m), (**c**) peak wave period (s), (**d**) peak wave direction (°) and (**e–h**) surface weather map at 12:00 UTC from 4 to 7 January. Cold fronts are in blue lines with triangles on the warm side of the front. Low-pressure and high-pressure areas are denoted with L and H, respectively. Green patches are areas experiencing rainfall; (**i**) wind vectors from the station WS. The arrows indicate the air flow velocity or the direction that the air particle is taking. The red vertical dashed lines indicate the timing of the cold fronts.
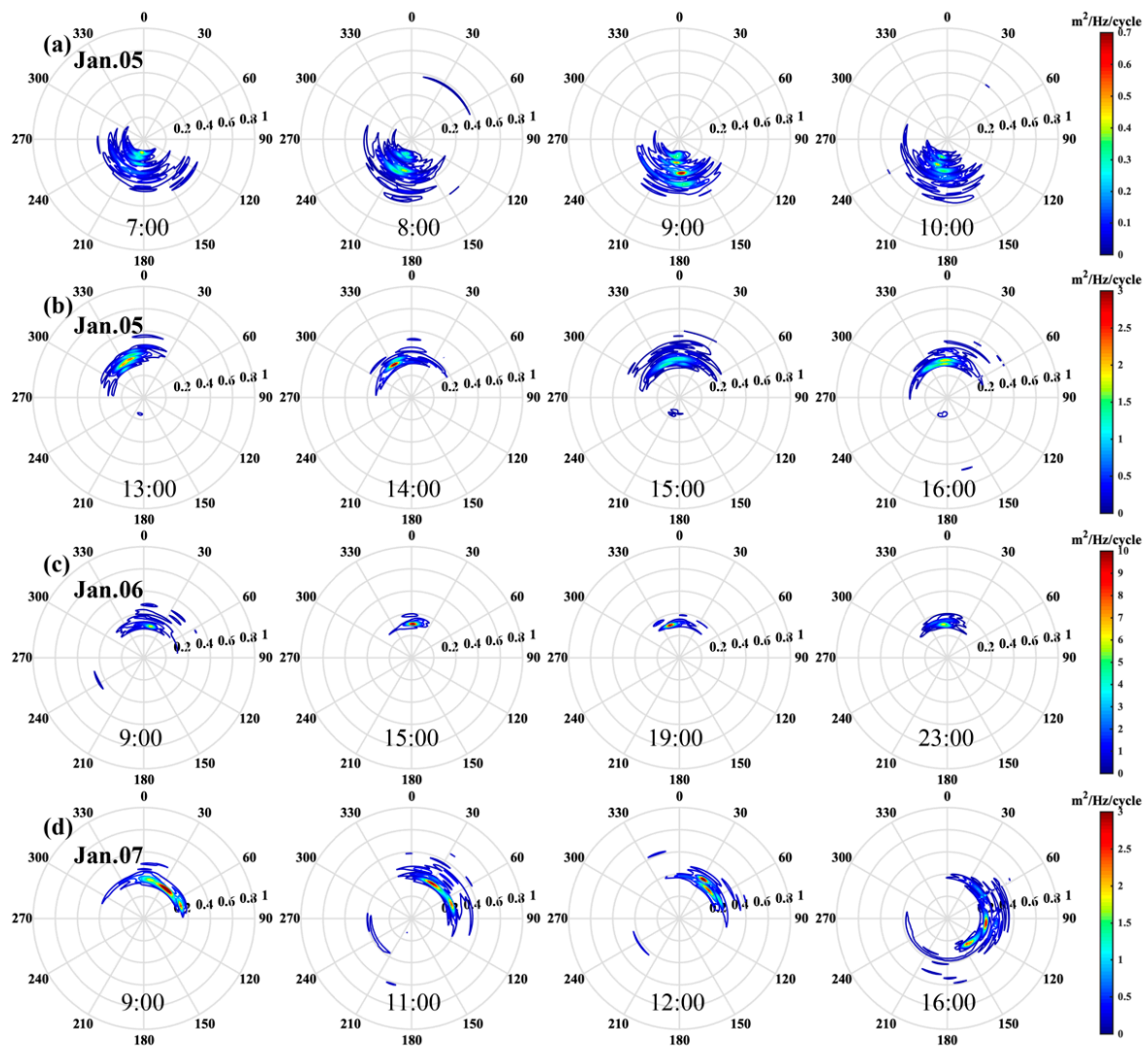
Figure 7. Hourly directional wave spectrum, as observed by the CSI 3 in the Case I. The 2-D directional spectra are shown in polar contours. (**a**) the prefrontal phase, (**b**) frontal passage phase (**c**,**d**) postfrontal phase from 5 to 7 January .

Case II is an arctic surge associated atmospheric cold front, which came from the north and moved to the south (see Figure 8f,g). In this example, wind speeds were less than 6 ms^{-1} in the prefrontal phase, and became stronger when the cold front passed. The maximum wind speed occurred at 5:00 UTC on 22 March (Figure 8a). Figure 8b shows the time series of the significant wave height from 20 to 23 March. The correlation coefficient between the wind speed at WS and wave height at CSI 3 is 0.68. The maximum value of the wave height was 0.79 m, and the extreme wave heights lasted for more than a day (26 h). Northly winds from onshore have short fetches. The peak wave periods in the prefrontal phase were larger than those in the frontal passage and postfrontal phases (Figure 8c). Figure 8d shows that the peak wave direction was north in the frontal phase and rotated clockwise. The wind direction rotated clockwise in the frontal and postfrontal phases. After the frontal passage, the northerly wind decreases rapidly and decreased by 7 ms^{-1} within 7 h (Figure 8i).
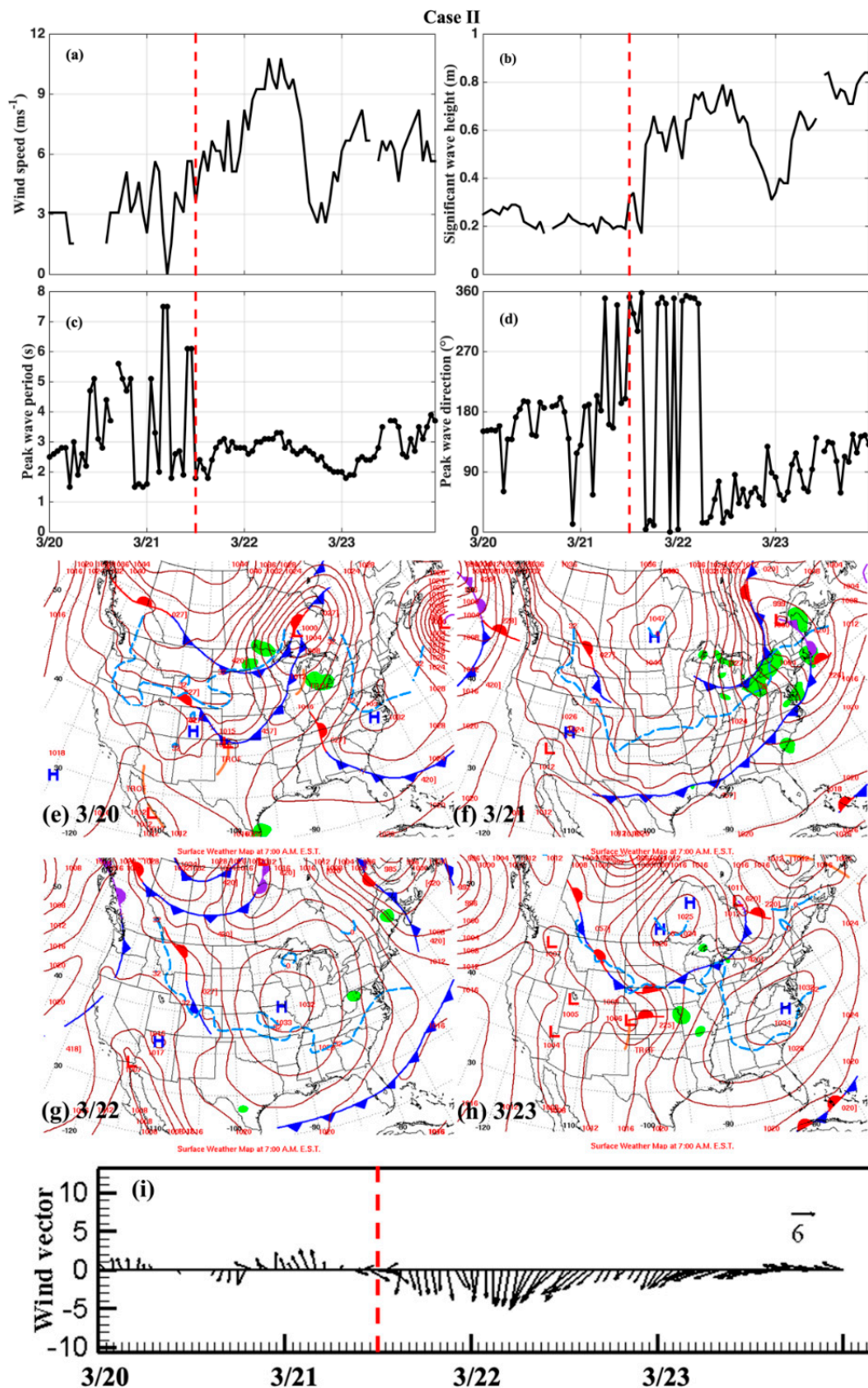
Figure 8. Case II: Time series of (**a**) wind speed (ms^{-1}), (**b**) significant wave height (m), (**c**) peak wave period (s), (**d**) peak wave direction (°), (**e**–**h**) surface weather map on 12:00 UTC from 20 to 23 March and (**i**) wind vectors from the station WS. The red vertical dashed lines indicate the timing of the cold fronts.

Figure 9 shows the directional wave spectra of Case II. The wave spectrum changed faster than Case I. In the prefrontal phase, the wave spectrum was distributed in all directions and was multi-modal in frequency. The characteristics of the spectrum in the prefrontal phase were different from that of Case I, and the peak energy was much weaker. At 6:00 UTC on 21 March, swell waves came from northeast, and a peak with low frequency came from the south. Two other peaks with high frequency distributed in the same direction (southeast). Five hours later at 11:00 UTC, wave energy disappeared in the north, and waves had different periods and amplitudes but similar approach directions (Figure 9a). When the cold front passed, the wave energy in the south quadrant decayed under the influence of the north–northwest wind field, and the spectrum became mono-modal at low frequencies (Figure 9b). The maximum wave directional spectrum occurred at low frequency at 7:00 UTC on 22 March during the postfrontal phase, and the value was 5 m^2/Hz/cycle (Figure 9c). Figure 9d shows that the direction of peak wave directional spectrum rotated clockwise and the wave energy reduced quickly. The swell appeared in the south first, and the wave spectrum was distributed in all directions with multiple peaks on the diagram at 20:00 UTC on 22 March.
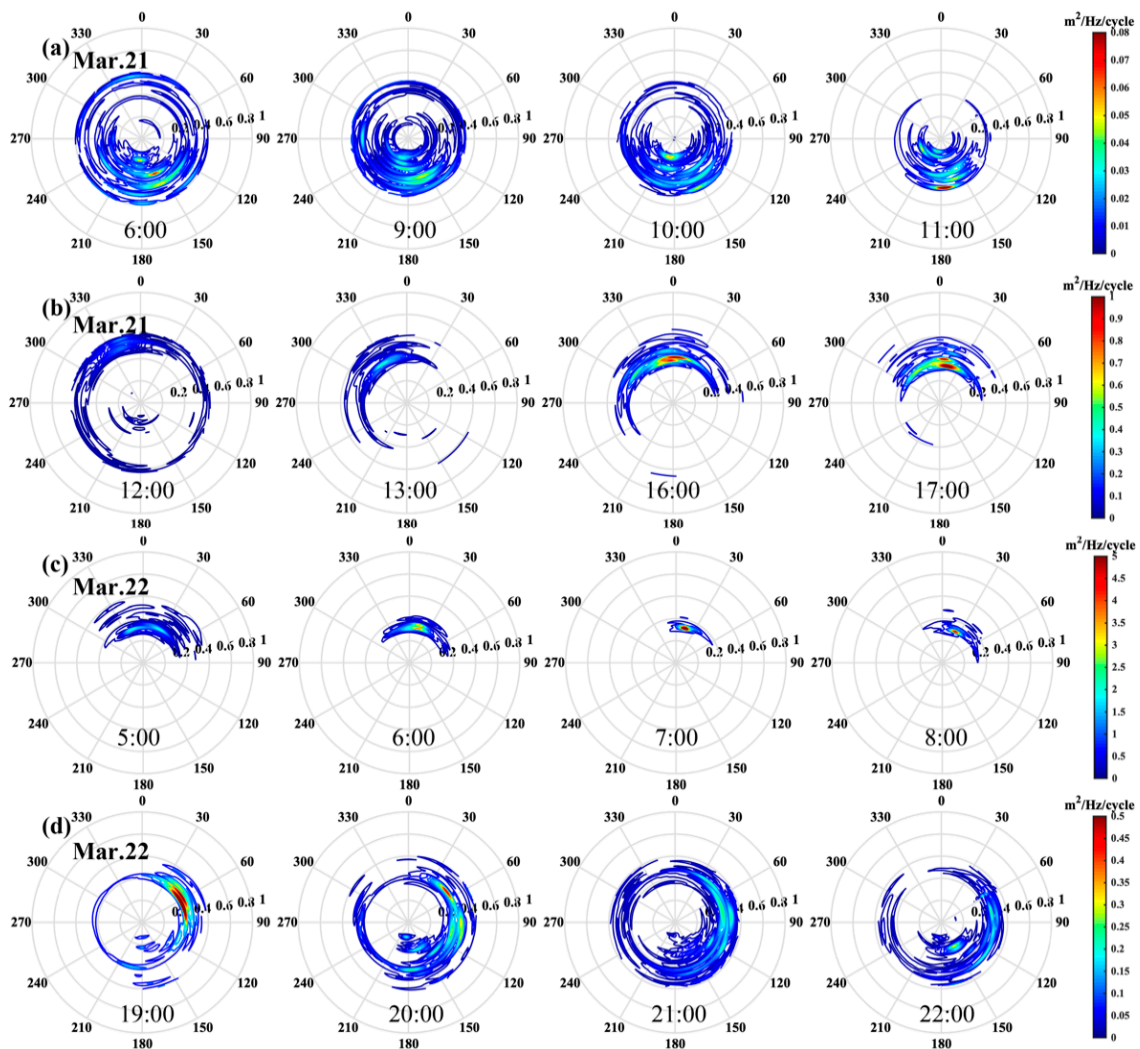

Figure 9. Hourly directional wave spectrum as observed by CSI 3 in the Case II. The 2-D directional spectra are shown in polar contours. (**a**) the prefrontal phase, (**b**) frontal passage phase (**c**,**d**) postfrontal phase from 21 to 22 March.

The cold front of Case III is the same as that of Case I, but the direction of the front was from the west to east. This cold front also had strong prefrontal southerly winds (Figure 10i). This migrating

cyclone was accompanied by a strong low-pressure system on 24 November (Figure 10f). Data from stations CSI 3 and CSI 6 (red stars in Figure 1) all captured the passage of cold front. There is a strong signal of cold front passage indicated by a rapid drop in air temperature by as much as 18 °C (Figure 3a). The minimum wind speed was 2.57 ms^{-1} on 24 November when the cold front passed. Sixteen hours later at 5:00 UTC, shown in Figure 10a, the wind speed increased to 14.39 ms^{-1}. During the next 20 h, wind speed dropped to 1.54 ms^{-1}. The wind directions rotated clockwise (Figure 10i). The winds were coming from the west when cold front passed the region. The wind directions changed to north on 23 November, associated with a high-pressure system (anti-cyclone) moving toward the east. The correlation coefficients between wind speed at WS and wave height at stations CSI 3 and CSI 6 are 0.64 and 0.73, respectively. In this case, the wind direction changed quickly and the wind fetch was short, so that the extreme wave height lasted for a shorter time. The maximum wave height reached 2.27 (CSI 6) and 0.86 m (CSI 3) at 1:00 UTC on November 25 (Figure 10b). During these hours, the wave height at CSI 6 was larger than that at CSI 3. On 26 November, the significant wave heights at two stations decreased to about 0.5 m. Figure 10c displays that the peak wave period at CSI 6 was longer than that at the CSI 3 in the frontal phase. On 26 November, the peak wave periods became the same at both stations. Figure 10d shows that the peak wave direction in the prefrontal phase was the same at both stations. On 25 November, the peak wave direction at CSI 3 changed to that from the north.

The observed 2-D directional wave spectra generated by the cold front at the two stations are shown in Figure 11. It can be observed that the wave energy propagation processes in different water depths are different. Figure 11a shows the directional wave spectra at the two stations in the prefrontal phase. The front associated with the migrating cyclone had strong prefrontal southerly winds, and the wave energy was stronger at CSI 3 than that in Case II. For CSI 3, the wave energy spread across a wide range frequency between 0.2 and 0.6 Hz. For CSI 6, the wave energy changed in low frequency and the peak value of spectrum was 8 m^2/Hz/cycle. The dominant wave energy came from the south and transferred to other lower frequencies. Figure 11b displays the time of direction of wave energy at CSI 3 transferred to the west before CSI 6. The maximum wave spectrum (2.5 m^2/Hz/cycle) at CSI 3 appeared at 18:00 UTC on 24 November and had dominant direction at 210°. The maximum wave spectrum (25 m^2/Hz/cycle) at the CSI 6 appeared in the same direction as at CSI 3 at 3:00 UTC on 25 November (Figure 11c). Multiple peaks appeared on the diagram in the postfrontal phase at both stations. However, lower frequency swells were dominant at CSI 6. Wind waves at CSI 3 rotated further to the southeast and centered at 120°. In the south, swells are produced by the southeast wind (Figure 11d). This shift in direction of the energy spectra in the postfrontal phase was attributed to the veering of wind direction and to the refraction of Marsh Island on waves.

Occasionally, an atmospheric cold front on the coast of Louisiana occurs with the presence of a tropical storm. In Case IV, the cold front came from the northwest (Figure 12f), associated with a migrating cyclone. Figure 12e shows that the tropical storm Frances (2004) was located east of the Louisiana coast. There were fairly strong prefrontal northeasterly winds and wind directions rotated counterclockwise before 8 September (Figure 12i). Due to the dual effects of cold fronts and tropical storm, the wind speed remained above 5 ms^{-1} from 6 to 8 September (Figure 12a). However, the mean wave height at CSI 3 was 0.27 m and the maximum valued 0.55 m. The mean wave height at CSI 6 was 0.74 m and the maximum value was 1.21 m. Wave heights of Case IV were obviously smaller than the first three cases (Figure 12b). The correlation coefficients between wind speed at WS and wave height at stations CSI 3 and CSI 6 are 0.35 and 0.51, respectively. There was a slight difference in the peak wave periods at the two stations (Figure 12c). CSI 6 was closer to the tropical storm than CSI 3, and the peak wave direction was from the east in the prefrontal phase at CSI 6. The *Dp* at CSI 3 changed significantly during this period and rotated clockwise in the postfrontal phase (Figure 12d). The variation of *Dp* at CSI 3 was similar to the wind direction (Figure 12i) in the postfrontal phase.
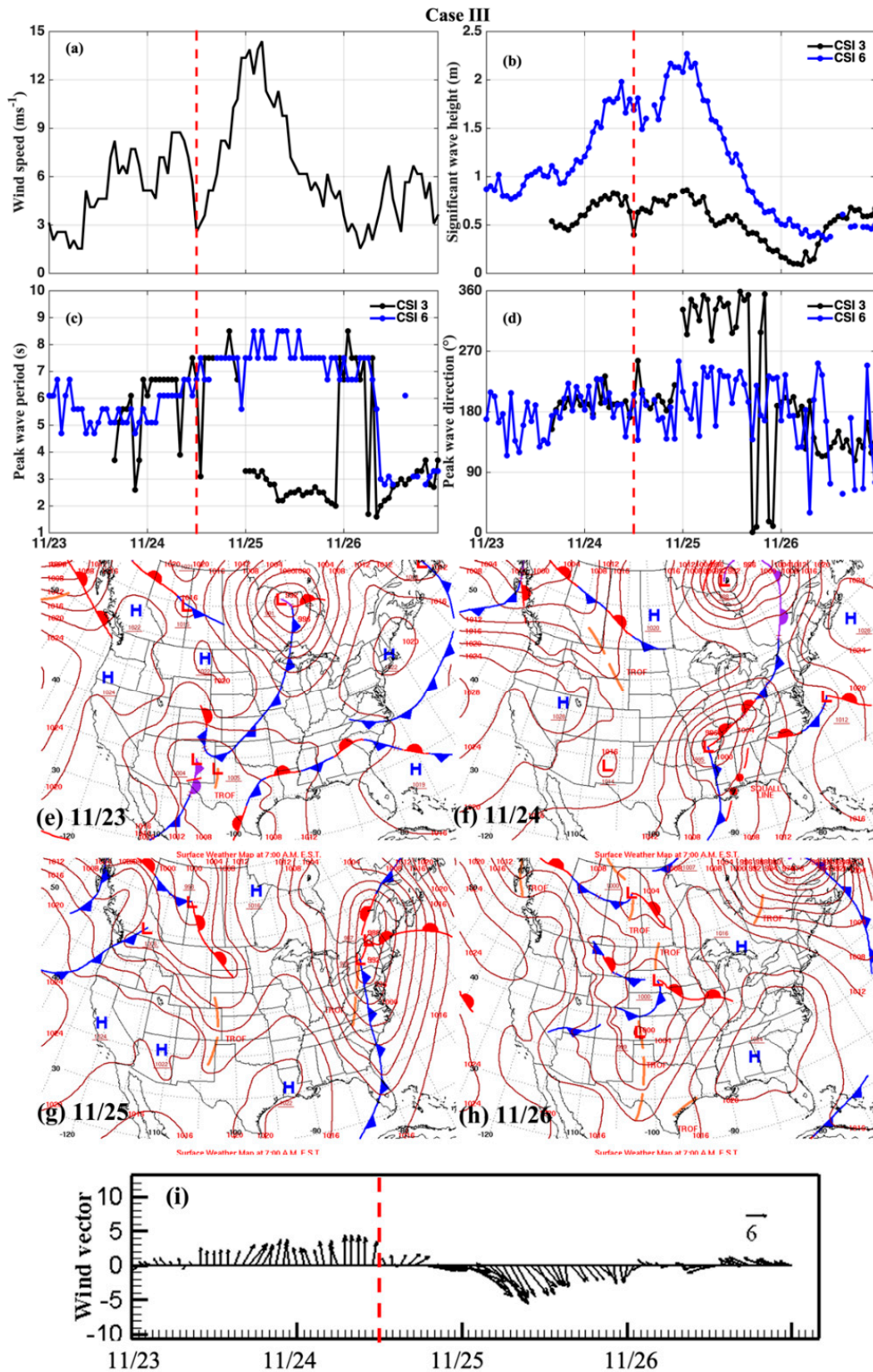
Figure 10. Case III: Time series of (**a**) wind speed (ms^{-1}) from the station WS, (**b**) significant wave height (unit: m), (**c**) peak wave period (s), (**d**) peak wave direction (°), waves observed by CSI 6 are plotted in blue lines and observed by CSI 3 are plotted in black lines, (**e**–**h**) surface weather map on 12:00 UTC from 23 to 26 November and (**i**) wind vectors from the station WS. The red vertical dashed lines indicate the timing of the cold fronts.
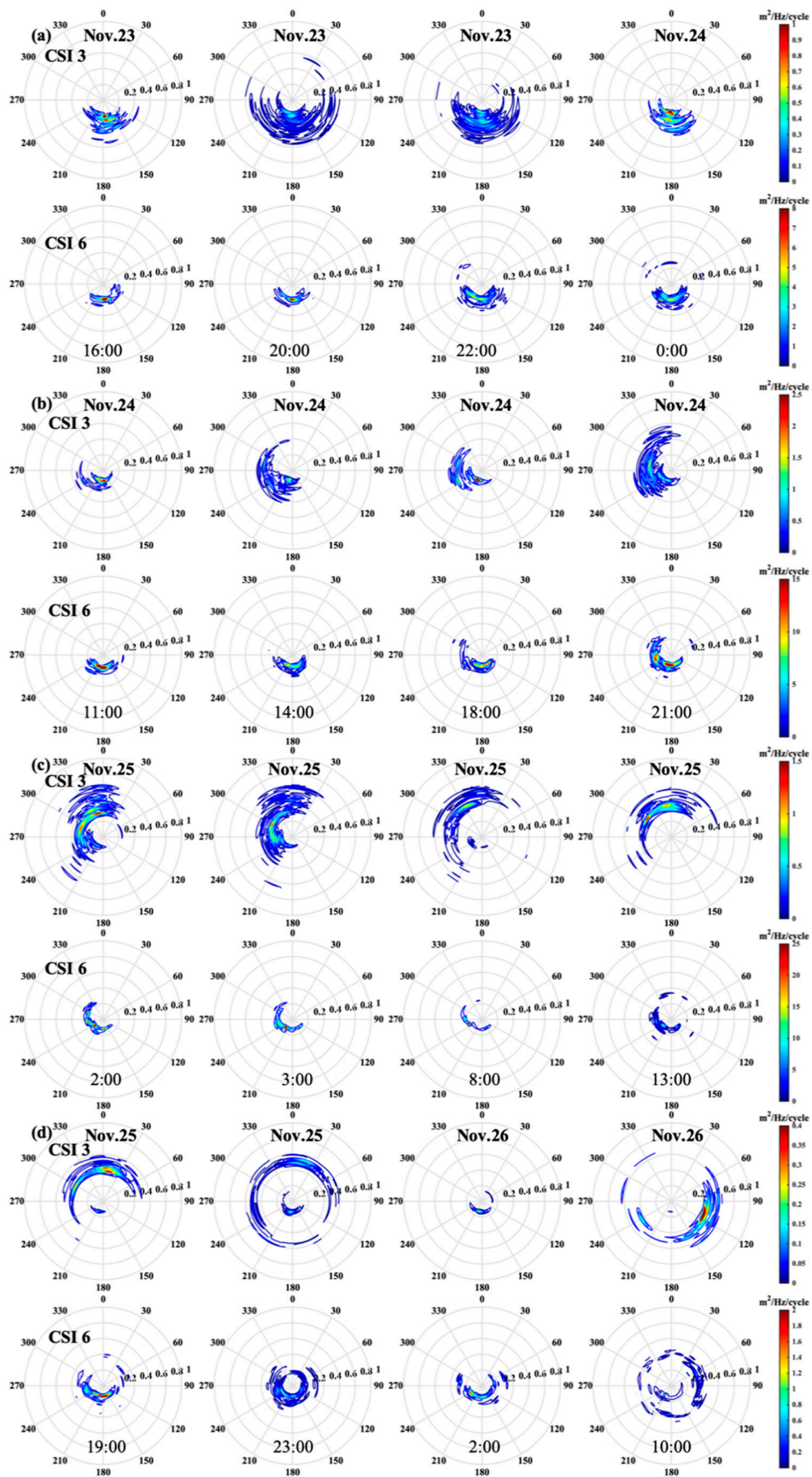
Figure 11. Hourly directional wave spectrum as observed by CSI 3 and CSI 6. The circles indicate the wave frequency from the center out with 0.1 Hz intervals. (**a**) Prefrontal phase, (**b**) frontal passage phase (**c**,**d**) postfrontal phase from 23 to 26 November.
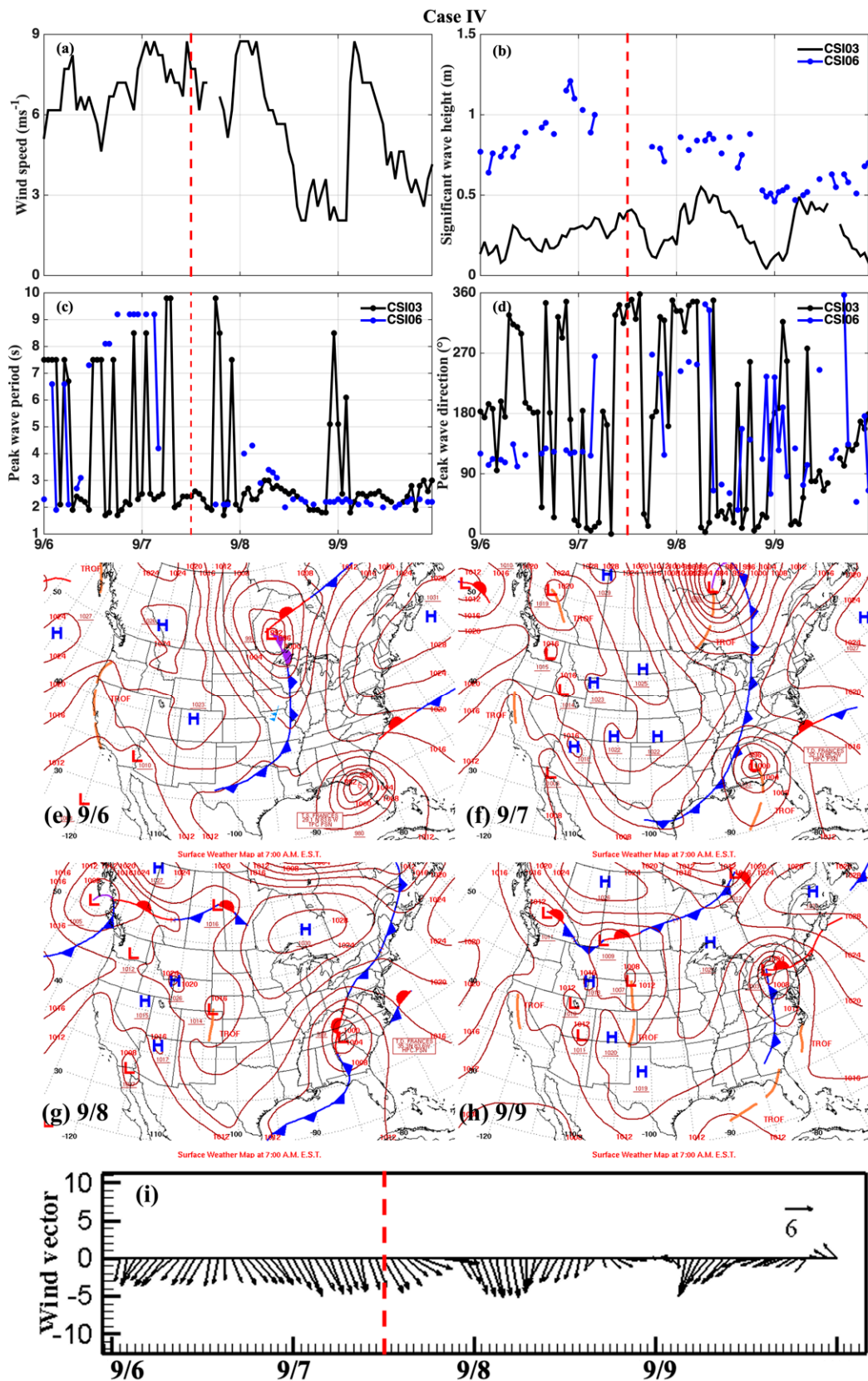
Figure 12. Case IV: Time series of (**a**) wind speed (ms^{-1}), (**b**) significant wave height (m). (**c**) peak wave period (s), (**d**) peak wave direction (°), (**e–h**) surface weather map on 12:00 UTC from 6 to 9 September and (**i**) wind vectors from the station WS. The red vertical dashed lines indicate the timing of the cold fronts.

Figure 13 displays the directional wave spectra at CSI 3 under the influence of this complex weather system. As CSI 3 is located 18 km south of Marsh Island, the limited fetch with such a proximity to land and shallow waters would affect the wave spectra. In the prefrontal phase, wave energy at short periods rotated clockwise from the northwest to the northeast. It was mainly mono-modal due to the long distance from the tropical storm center. Low-frequency waves from the GoM appeared in the south direction (Figure 13a). When the front passed, all four diagrams were mono-modal, and the wave energy in the south quadrant decayed (Figure 13b). The maximum wave directional spectrum in the first two phases reached 0.6 m^2/Hz/cycle. On 8 September, the direction of the wave spectra rotated clockwise from the northwest to northeast under the influence of the cold front. The peak energy was induced by the high-frequency local wind and the peak value of directional spectrum increased to 1 m^2/Hz/cycle (Figure 13c). The wave energy was distributed in all quadrants in the four spectra. The dominant wave energy transferred to the northwest quadrant (Figure 13d).
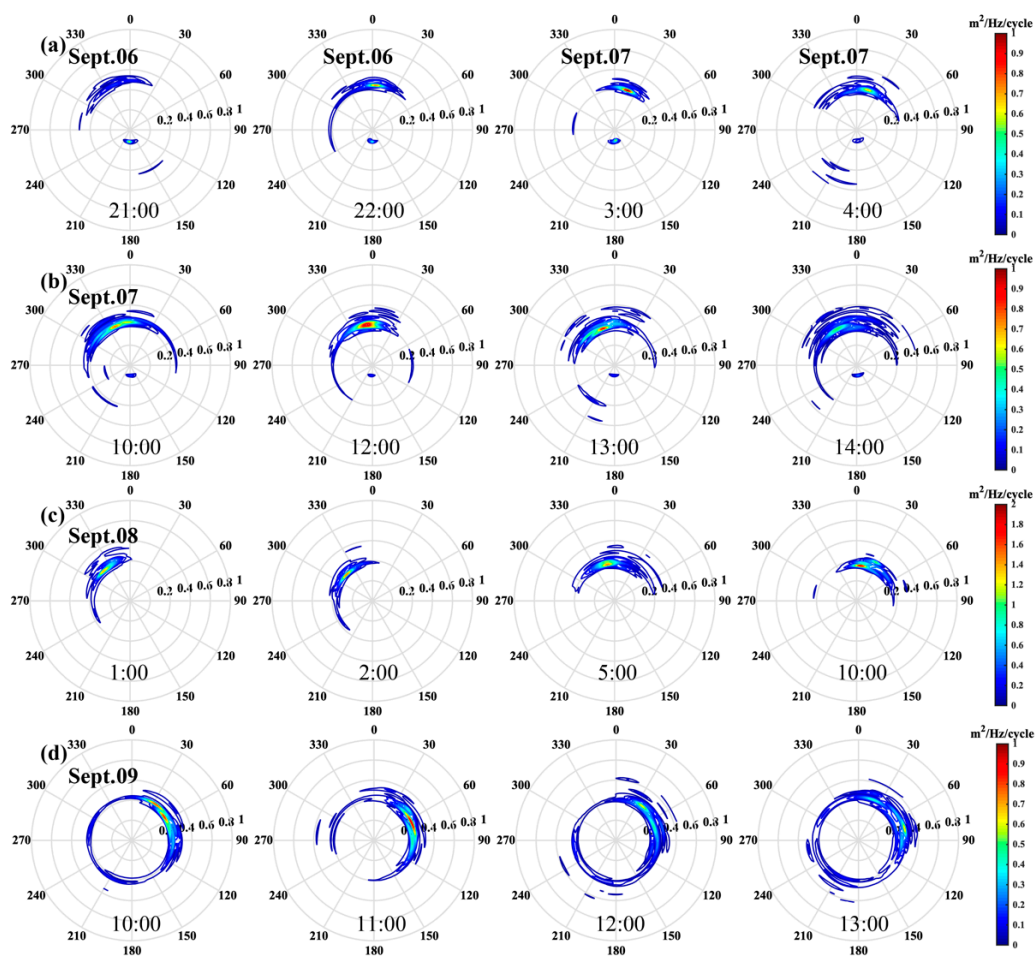

Figure 13. Hourly directional wave spectrum as observed by CSI 3 in the Case IV. The 2-D directional spectra are shown in polar contours. (**a**) Prefrontal phase, (**b**) frontal passage phase (**c**,**d**) postfrontal phase from September 6 to 9.

4. Discussion

As in previous studies over coastal Louisiana, waves influenced by atmospheric cold front are further discussed (e.g., [4,37]). Generally, due to the high sea-state during storms and the cost associated with any data collection activities, the in-situ measurements of waves, not to mention directional waves, are quite limited. Therefore, long-term continuous observation data are extremely valuable. From the results discussed in Section 3, analyzing a relatively long time series of directional waves, it is found that the intra-seasonal change scale of waves is greatly affected by the cold front.

Four cases are analyzed in Section 3.2. The wave parameter characteristics for each case in three front phases are shown in Table 2. Clearly, AS storms have lower average significant wave height, wind speed and shorter peak wave period than MC storms. The MC storm coming from the northwest has the most energetic waves among the four cases, with peaks in *Hs* occurring during both the frontal passage and postfrontal phases. Peaks in *Hs* generated by the MC storm coming from the west occur in the prefrontal and frontal passage phases. Wave response to the MC storm is more complex than that for the AS storm, due to the fact that complex weather pressure systems often accompany MC storms.

Table 2. Characteristics of wave parameters in three phases.

Case	Type	Moving Direction	Characteristics of Parameters					
I	MC storm	NW	Wind speed (mean; unit: ms^{-1})			*Hs* (mean; unit: m)		
			prefrontal	Frontal passage	postfrontal	prefrontal	Frontal passage	postfrontal
			4.9	8.2	6.4	0.35	0.72	0.71
			Tp (mean; unit: s)			Spectrum density (peak; unit: m^{2}Hz-^{1}cycle^{-1})		
			prefrontal	Frontal passage	postfrontal	prefrontal	Frontal passage	postfrontal
			4.5	3.3	2.9	0.3–0.7	3–5	3–10
II	AS storm	N	Wind speed (mean; unit: ms^{-1})			*Hs* (mean; unit: m)		
			prefrontal	Frontal passage	postfrontal	prefrontal	Frontal passage	postfrontal
			3.2	7.5	6.1	0.22	0.58	0.63
			Tp (mean)			Wave spectrum density (peak; unit: m^{2}Hz-^{1}cycle^{-1})		
			prefrontal	Frontal passage	postfrontal	prefrontal	Frontal passage	postfrontal
			3.5	2.8	2.7	0.06–0.08	1–5	0.3–0.5
III	MC storm	W	Wind speed (mean; unit: ms^{-1})			*Hs* of CSI 3 (CSI 6) (mean; unit: m)		
			prefrontal	Frontal passage	postfrontal	prefrontal	Frontal passage	postfrontal
			5.3	9.3	4.6	0.64(1.19)	0.68(1.81)	0.40(0.60)
			Tp of CSI 3 (CSI 6) (mean; unit: s)			Wave spectrum density (peak; unit: m^{2}Hz-^{1}cycle^{-1})		
			prefrontal	Frontal passage	postfrontal	prefrontal	Frontal passage	postfrontal
			5.8(5.6)	4.8(7.5)	3.7(5.9)	1–2.5 (7–12)	1.5–2.5 (15–25)	0.4–1 (1.5–2)
IV	MC storm (Tropical Storm)	NW	Wind speed (mean; unit: ms^{-1})			*Hs* of CSI 3 (CSI 6) (mean; unit: m)		
			prefrontal	Frontal passage	postfrontal	prefrontal	Frontal passage	postfrontal
			7.0	7.1	4.20	0.24(0.90)	0.34(0.81)	0.26(0.60)
			Tp of CSI 3 (CSI 6) (mean; unit: s)			Wave spectrum density (peak; unit: m^{2}Hz-^{1}cycle^{-1})		
			prefrontal	Frontal passage	postfrontal	prefrontal	Frontal passage	postfrontal
			4.4(6.4)	3.2(2.9)	2.8(2.2)	0.6–1	1.5–2	0.6–1

The measured 2-D wave direction spectrum data are useful in determining the evolution of waves during cold fronts. The wave spectrum shows wave energy and direction variation as the wind changes in magnitude and direction when the front passes the region. In comparison, Jose et al. [22] studied wave propagation under a single cold front over ship shoal along the Louisiana coast in April 2005. Kobashi et al. [38] studied the impact of a cold front on the mud fluid transport. In this study, however, we analyzed hourly 2-D wave directional spectrum variability observed at the WAVICS stations during the passage of four typical cold fronts in one year (2004). The hourly spectrum shows detailed characteristics of the direction and frequency of wave energy. The propagation directions of wave energy generated by the storms are characterized by clockwise rotation. The long-period northerly swell wave and the short-period southerly storm wave contribute greatly to the energy spectrum. Both of these waves mostly appear during of the postfrontal phase. AS storms are mainly short-period southerly waves in the postfrontal phase [33]. Unlike hurricanes, which are usually characterized by complex, bimodal spectra [16], the observed spectrum is essentially mono-modal during the frontal passage.

5. Conclusions

Cold fronts play an essential role in coastal waves of the Bays of Louisiana. Frequent cold front events during a year cause relatively strong recurring winds and waves with similar characteristics in coastal Louisiana. The temporal variation is an essential part of the wave dynamics. Exploring the temporal variations of wave height and peak wave period can help us to better understand the wave response to weather events. Studying long-term series of in-situ data is helpful for ocean forecasting. Wave height and peak wave period have a significant intra-seasonal variation in coastal Louisiana. During the cold front passing, wind speed, wave height and peak wave period all increase.

This work analyzed wave data observed at WAVCIS stations CSI 3 and CSI 6 in order to understand directional wave evolution in coastal Louisiana water during cold front passages. A total of 37 atmospheric cold frontal events occurred in the coastal Louisiana in 2004 (excluding May through August), five of which were AS storms, while the other 32 were MC storms. By filtering the time series, intra-seasonal temporal variations of waves are related to frequent cold front activities. The air pressure and wave field share an oscillation period of about 3–7 days [8].

Two storm types and their associated wave responses are discussed in this study. The effects from two types of cold fronts passing coastal Louisiana on the wave field were studied. The peak wave period increases in the prefrontal phase and the variation of the peak wave direction is rotating clockwise during the cold front events. Case I, Case III and Case IV are associated with a migrating cyclone. Case II is an arctic surge associated atmospheric cold front. During frontal passages, the mean *Hs* is 0.72 m for Case I and 0.58 m for Case II. AS storms have lower average significant wave height than MC storms. After comparison, the wave heights generated by cold front coming from the west change more quickly than those by other passing cold fronts. Wave characteristics measured at different stations with different depths are different. The MC storm comes from the west in Case II, which generates an average wave height of 1.81 m at CSI 6. The average wave height is 0.68 m at CSI 3 in the frontal passage phase. Cold front-induced wave energy at the station with deeper water (CSI 6) is dominated by lower frequencies. The variation of the 2-D directional wave spectrum during the cold front events shows that the largest spectral density is distributed at low frequency in the postfrontal phase.

Author Contributions: Conceptualization, C.L.; methodology, Y.C. and C.L.; software, Y.C.; formal analysis, Y.C.; investigation, Y.C.; writing—original draft preparation, Y.C.; writing—review and editing, C.L. and Y.C.; funding acquisition, C.L. and C.D. All authors have read and agreed to the published version of the manuscript.

References

1. Lopez, G.; Conley, D.C. Comparison of HF Radar Fields of Directional Wave Spectra Against In Situ Measurements at Multiple Locations. *J. Mar. Sci. Eng.* **2019**, *7*, 271. [CrossRef]

2. Penland, S.; Roberts, H.H.; Williams, S.J.; Sallenger, A.H., Jr.; Cahoon, D.R.; Davis, D.W.; Groat, C.G. Coastal land loss in Louisiana. *Gulf Coast Assoc. Geol. Soc. Trans.* **1990**, *40*, 685–699.

3. Stone, G.W.; Williams, S.J.; Burruss, A.E. Louisiana's barrier islands: An evaluation of their geological evolution, morphodynamics and rapid deterioration. *J. Coast. Res.* **1997**, *13*, 591–592.

4. Guo, B.; Subrahmanyam, M.V.; Li, C. Waves on Louisiana Continental Shelf Influenced by Atmospheric Fronts. *Sci. Rep.* **2020**, *10*, 1–9. [CrossRef]

5. Li, C.Y.; Roberts, H.; Stone, G.W.; Weeks, E.; Luo, Y.X. Wind surge and saltwater intrusion in Atchafalaya Bay during on- shore winds prior to cold front passage. *Hydrobiologia* **2011**, *658*, 27–39. [CrossRef]

6. Roberts, H.H.; Huh, O.K.; Hsu, S.A.; Rouse, L.J.; Rickman, D. Winter storm impacts on the Chenier plain coast of southwestern Louisiana. *Trans. Gulf Coast Assoc. Geol. Soc.* **1989**, *39*, 515–522.

7. Chaney, P.L. Extratropical Storms of the Gulf of Mexico and Their Effects along the Northern Coast of a Barrier Island: West Ship Island, Mississippi. Ph.D. Thesis, Louisiana State University, Baton Rouge, LA, USA, 1999.

8. Li, C.Y.; Huang, W.; Wu, R.H.; Sheremet, A. Weather induced quasi-periodic motions in estuaries and bays: Meteorological tide. *China Ocean Eng.* **2020**, *34*, 1–15. [CrossRef]

9. Maresca, J.W., Jr.; Georges, T.M. Measuring rms wave height and the scalar ocean wave spectrum with HF skywave radar. *J. Geophys. Res. Oceans* **1980**, *85*, 2759–2771. [CrossRef]

10. Doyle, J.D. Coupled ocean wave/atmosphere mesoscale model simulations of cyclogenesis. *Tellus A* **1995**, *47*, 766–778. [CrossRef]

11. Dragani, W.C. Numerical experiments on the generation of long ocean waves in coastal waters of the Buenos Aires province, Argentina. *Cont. Shelf Res.* **2007**, *27*, 699–712. [CrossRef]

12. Zhao, P.; Jiang, W. A numerical study of storm surges caused by cold-air outbreaks in the Bohai Sea. *Nat. Hazards* **2011**, *59*, 1–15. [CrossRef]

13. Appendini, C.M.; Hernández-Lasheras, J.; Meza-Padilla, R.; Kurczyn, J.A. Effect of climate change on wind waves generated by anticyclonic cold front intrusions in the Gulf of Mexico. *Clim. Dyn.* **2018**, *51*, 3747–3763. [CrossRef]

14. Kita, Y.; Waseda, T.; Webb, A. Development of waves under explosive cyclones in the Northwestern Pacific. *Ocean Dyn.* **2018**, *68*, 1403–1418. [CrossRef]

15. Chaichitehrani, N.; Li, C.; Xu, K.; Allahdadi, M.N.; Hestir, E.L.; Keim, B.D. A numerical study of sediment dynamics over Sandy Point dredge pit, west flank of the Mississippi River, during a cold front event. *Cont. Shelf Res.* **2019**, *183*, 38–50. [CrossRef]

16. Hu, K.; Chen, Q. Directional spectra of hurricane-generated waves in the Gulf of Mexico. *Geophys. Res. Lett.* **2011**, *38*. [CrossRef]

17. Young, I.R.; Vinoth, J.; Zieger, S.; Babanin, A.V. Investigation of trends in extreme value wave height and wind speed. *J. Geophys. Res.* **2012**, *117*, 13. [CrossRef]

18. Hemer, M.A.; Fan, Y.; Mori, N.; Semedo, A.; Wang, X.L. Projected changes in wave climate from a multi-model ensemble. *Nat. Clim. Chang.* **2013**, *3*, 471–476. [CrossRef]

19. Cao, Y.; Dong, C.; Uchiyama, Y.; Wang, J.; Yin, X. Multiple-scale variations of wind-generated waves in the Southern California Bight. *J. Geophys. Res. Oceans* **2018**, *123*, 9340–9356. [CrossRef]

20. Stone, G.W.; Kumar, B.P.; Sheremet, A.; Watzke, D. Complex morpho-hydrodynamic response of estuaries and bays to winter storms: North-central Gulf of Mexico. In *High Resolution Morphodynamics and Sedimentary Evolution of Estuaries*; Springer: Dordrecht, The Netherlands, 2005; pp. 243–267.

21. Stone, G.W.; Liu, B.; Jose, F. Winter storm and tropical cyclone impacts on the short- term evolution of beaches and barriers along the northeastern Gulf of Mexico. In Proceedings of the Coastal Sediments '07, New Orleans, LA, USA, 13–17 May 2007; pp. 935–950.

22. Jose, F.; Kobashi, D.; Stone, G.W. Spectral wave transformation over an elongated sand shoal off south-central Louisiana, USA. *J. Coast. Res.* **2007**, *50*, 757–761.

23. Sorourian, S.; Huang, H.; Li, C.; Justic, D.; Payandeh, A.R. Wave dynamics near Barataria Bay tidal inlets during spring–summer time. *Ocean Model.* **2020**, *147*, 101553. [CrossRef]

24. Zhang, X. Design and Implementation of an Ocean Observing System: WAVCIS (Wave-Current-Surge Information System) and Its Application to the Louisiana Coast. Ph.D. Thesis, Louisiana State University, Baton Rouge, LA, USA, 2003.

25. *WavesMon User's Guide*; P/N 957-6148-00; RD Instruments: San Diego, CA, USA, 2011; p. 74.

26. Herbers, T.H.C.; Lentz, S.J. Observing directional properties of ocean swell with an acoustic Doppler current profiler (ADCP). *J. Atmos. Ocean. Technol.* **2010**, *27*, 210–225. [CrossRef]

27. Hoffman, R.N.; Leidner, S.M.; Henderson, J.M.; Atlas, R.; Ardizzone, J.V.; Bloom, S.C. Bloom. A two-dimensional variational analysis method for NSCAT ambiguity removal: Methodology, sensitivity, and tuning. *J. Atmos. Ocean. Technol.* **2003**, *20*, 585–605. [CrossRef]

28. Emery, W.J.; Thomson, R.E. Data analysis methods in physical oceanography. *Estuaries* **2001**, *80*, 638.

29. Cooley, J.W.; Tukey, J.W. An Algorithm for the Machine Computation of the Complex Fourier Series. *Math. Comput.* **1965**, *19*, 297–301. [CrossRef]

30. Willmott, C.J. On the validation of methods. *Phys. Geogr.* **1981**, *2*, 184–194. [CrossRef]

31. Li, C.; Weeks, E.; Milan, B.; Huang, W.; Wu, R. Weather Induced Transport through a Tidal Channel Calibrated by an Unmanned Boat. *J. Atmospheric Ocean. Technol.* **2018**, *35*, 261–279. [CrossRef]

32. Roberts, H.H.; Huh, O.K.; Hsu, S.A.; Rouse, L.J., Jr.; Rickman, D. *Impact of Cold- Front Passages on Geomorphic Evolution and Sediment Dynamics of the Complex Louisiana Coast. Coastal Sediments '87, Proceedings of a Specialty Conference, New Orleans, Louisiana, 12–14 May 1987*; American Society of Civil Engineers: New York, NY, USA, 1987; pp. 1950–1963.

33. Pepper, D.A.; Stone, G.W. Hydrodynamic and sedimentary responses to two contrasting winter storms on the inner shelf of the northern gulf of mexico. *Mar. Geol.* **2004**, *210*, 43–62. [CrossRef]

34. Eldeberky, Y. Nonlinear transformation of wave spectra in the nearshore zone. *Oceanogr. Lit. Rev.* **1997**, *4*, 297.

35. Van de Voorde, N.E.; Dinnel, S.P. Observed directional wave spectra during a frontal passage. *J. Coast. Res.* **1998**, *14*, 337–346.

36. Herbers, T.H.C.; Elgar, S.; Guza, R.T. Directional spreading of waves in the nearshore. *J. Geophys. Res. Ocean.* **1999**, *104*, 7683–7693. [CrossRef]

37. Feng, Z.X.; Li, C.Y. Cold-front-induced flushing of the Louisiana Bays. *J. Mar. Syst.* **2010**, *82*, 252–264. [CrossRef]

38. Kobashi, D.; Jose, F.; Stone, G.W. Impacts of fluvial fine sediments and winter storms on a transgressive shoal, off south-central Louisiana, USA. *J. Coast. Res.* **2007**, *23*, 858–862.